CEAS Aeronautical Journal
https://doi.org/10.1007/s13272-023-00676-9

ORIGINAL PAPER

High-resolution vibroacoustic characterization of DLR's Falcon 2000LX ISTAR aircraft

René Winter[1] · Marco Norambuena[1] · Julian Sinske[1] · Sebastian Zettel[1]

Received: 4 May 2023 / Revised: 18 July 2023 / Accepted: 31 July 2023

Abstract

In the framework of CleanSky2's Airframe project DA9, engine tonal noise is a cooperation between Dassault Aviation and DLR. The project aims to enhance the understanding and mitigation of engine-related tonal noise in the aircraft cabin. The presented work was done to get an in-depth understanding of the vibroacoustic behavior of DLR's Falcon 2000LX ISTAR aircraft. A two and a half weeks long vibroacoustic ground test was conducted utilizing artificial shaker excitation and operational engine excitation. The responses were measured using a roving grid of accelerometers at more than 1200 positions, meaning a subset of about 250 sensors were installed at every given time and then moved along the fuselage in a predetermined way to get a high-resolution measurement of aircrafts fuselage. The accelerometer data were than processed to show operational deflections shapes and calculate experimental structural intensity vector fields to analyze the energy transfer through the structure for optimized placement of active or passive counter measures. Specifically, the transport of tonal frequencies generated by the engines was analyzed.

Keywords Vibroacoustic · Ground vibration test · Structure intensity analysis

Abbreviations

AFL	Acoustic flight-LAB
CDM	Central difference method
EMA	Experimental modal analysis
FE	Finite elements method
ISTAR	In-flight systems and technology airborne research
ODS	Operational deflection shape
PCA	Principal component analysis
PC	Principal component
PFS	Principal field shape
PODS	Principal operational deflection shape
STI	Structural intensity
SVD	Singular value decomposition

List of symbols

$[H]_{Band}$	Band limited frequency response matrix
M	Element bending moments
N	Normal element forces
n_F	Indices of frequency bins
n_S	Indices of sensors
ω	Angular frequency
P	Power flow
[PS]	Matrix of principle shapes
Q	Element transversal forces
$[\Sigma]$	Matrix of singular values
T	Beam element torsion
[U]	Matrix of left singular values
[V]	Matrix of right singular values
v	Velocity

Marco Norambuena, Julian Sinske, and Sebastian Zettel have equally contributed to this work.

✉ René Winter
rene.winter@dlr.de

Marco Norambuena
marco.norambuena@dlr.de

Julian Sinske
julian.sinske@dlr.de

Sebastian Zettel
sebastian.zettel@dlr.de

[1] Deutsches Zentrum für Luft-und Raumfahrt e.v., Institut für Aeroelastik, Bunsenstr. 10, 37073 Göttingen, Germany

1 Introduction

Understanding and predicting the transfer of vibrations through an aircraft fuselage are a complicated task necessary to correctly predict cabin noise. The fuselage of an aircraft is built in a grid-like structure with longitudinal stringers and circumferential frames keeping the skin layer in place. This creates a mesh of possible paths for the vibration energy to travel along. In addition, there are several different possible vibration sources acting on the structure. Some broadband, like the turbulent boundary layer, others of a more distinct, tonal characteristic like vibrations caused by the engine fan rotations.

In the past several measurements on laboratory structures [1], on full-sized aircraft fuselage, component demonstrators [2] and on an A400M fuselage [3] have been conducted to gain insight into the specific problem of vibroacoustic transfer through light-weight structures and to further develop measurement techniques. Presented here is the first such measurement and analysis performed on a fully equipped aircraft and with the goal of analyzing a specific problem: The identification of vibrational energy transfer originating from the engines of an aircraft into the cabin. These vibrations show a strong tonal characteristic, and while their initial transfer path can be easily mapped from the engine to the pylon into the fuselage, their transfer via the ripped fuselage structure is more complicated.

To get a better understanding of the problem and to test possible solutions, the German Aerospace Center (DLR), in cooperation with Dassault Aviation, conducted a large-scale vibroacoustic measurement campaign on a research aircraft in March 2022. The aircraft in question was a Dassault Falcon 2000LX owned by DLR known as the ISTAR, an acronym for In-Flight Systems & Technology Airborne Research (see Fig. 1). The ISTAR is fitted with two rear mounted engines whose vibrational energy input into the structure was the primary focus of the measurement campaign.

Identifying the vibration transfer originating at these engines to the passenger cabin is one of the goals of the project the presented work is part of. Another goal, not presented here, was the acquisition of cabin noise characteristics used for the design of active noise reduction systems in the ongoing project. The test campaign was conducted by DLR's vibration testing team over the course of 2 weeks, where the vibration response of the fuselage structure was measured at 1310 individual sensor positions on the fuselage alone. Additional sensors were deployed to the pressure bulk head and the cabin floor.

After the test was conducted, the data were analyzed for its quality and several different analyses have been run to better understand the vibrational energy transport.

Parts of the methods presented in here were previously published at the INTER-NOISE conference in 2018 and 2022 (see [2, 4]). They are repeated and expanded upon to facilitate the comprehensibility of the results presented in chapter 3. Additionally, in [4], preliminary results of this test campaign were presented. Those do not overlap with what is shown here.

2 Methods

2.1 Vibroacoustic testing: equipment and methods

The engines and the vibration injected by the engines were the primary focus of the measurement campaign, being one of the aforementioned tonal vibration sources. A good tool for detailed analysis of power flow through the structure is the STI method. It requires very detailed, densely spaced measurement grids. In fact, higher the grid density the better [1]. It was, however, not feasible to measure the whole fuselage structure with a grid as dense as, for example, previously performed on the "Acoustic Flight-Lab" laboratory structure [2] due to time limitations factoring in when measuring an aircraft.

Fig. 1 The DLR ISTAR with sensor configuration C1 installed. The full measurement grid is marked on the fuselage by removable stickers. ©2022DLR

To achieve a maximum number of measurement positions with a limited number of sensors, a roving grid method is used. A detailed overview of the roving grid testing process applied can be found in [3]. At its core, the process subdivides the measurement grid into subsections optimized to utilize as many sensors as possible at once while also allowing for an easy installation of the subsection and subsequent grid configurations. The specifics of the subgrids depend on the accessibility of the structure on site, the available space for cable routing, etc. This test posed the additional complication of an installation to the outside of an already painted aircraft, making the precise localization of sensor positions very difficult and time consuming.

The Falcon 2000LX's relevant characteristics to sensor grid design for this project are: It has rear mounted engines, is 20.2 m long, and has a cabin width of 2.35 m. Starting from these, the sensor grid was designed with several goals in mind: An existing finite-element model of the aircraft needs to be verified, updated, and, especially for the fuselage section, refined for the higher frequency range. In addition, the data will be used to calculate structural intensities (see Sect. 2.3) to get an impression of the vibration energy flow through the fuselage. This energy flow should be considered both for artificial shaker excitation and operational vibrations caused by the engines. Within the scope of the projects time frame and the aircrafts accessibility, these goals could only be reached by compromising on some of them. It was decided to not use more than five subgrids of up to 300 sensors each, as more subgrids would most likely not be doable in the scheduled time and more sensors in parallel would exceed the limits of what was available.

The baseline finite-element model (FEM) of the ISTAR is a symmetric model derived from a half-shell model. While this is not perfectly true for the actual aircraft, it is sufficiently so in the rear half. Thus, the detailed measurements were limited to one half of the aircraft assuming symmetry. With these limits established, a measurement grid was designed using 1310 positions (see 3a) spread over five sensor configurations. In addition, a limited number of sensors used for verification purposes were installed on the other side of the aircraft (see Fig. 2b).

While previous measurements using sensors [2] used 15 sensors per skin field and surrounding stiffeners, this measurement is limited to six sensors per equivalent structure. This will of course limit the frequency up to which reliable information can be gathered from the data, but otherwise the goal of having data along most of the fuselage would not have been reached. The measurement of the operational excitation by the engines caused a different problem: The roving grid method was not a viable option as the installation time per configuration escalates. The sensors and their cables have to be secured so as to not being sucked into the engines. The aircraft has to be outside for the test. Depending upon the weather that is not always an option. It was decided to only measure a single configuration with running engines. This configuration is focused on the area around the pylon, to get a good understanding of the vibrations injected into the aircraft (see Fig. 3a).

The vibroacoustic testing was conducted using accelerometers as sensors and electromagnetic shakers for artificial excitation. Specifically, Kistler 8000M095 sensors were used. These have a viable frequency range of 0.5 Hz to 1 kHz, and their casing and sensor elements were selected for optimal performance and usability in a ground test campaign on aircraft [5]. The sensors have an individual weight of 10 g. The added distributed mass of 300 sensors and corresponding cables of 9 g/m will lead to a negligible downshift of response frequencies by a total added mass of approximately 10 kg distributed along a 10800 kg structure.

The artificial excitation was realized using TIRA TV 51120-MOSP shakers with bandlimited random excitation at 40-500 Hz. The measurement system used was a 480 (5×96) channel Simcenter SCADAS Mobile system, which controlled the excitation and was used to acquire time data. All further processing was done in custom software implemented in Matlab. More details regarding the general setup of the measurement system and the post-processing can be found in [3].

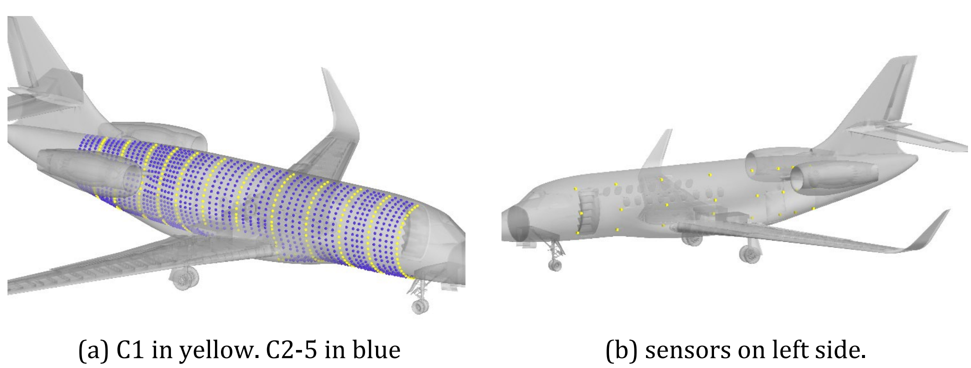

Fig. 2 Sensor configurations used during the test. The main test was done using five configurations C1–C5 which wore installed and measured sequentially (see **a**). Twenty-four sensors were permanently installed to the left side of the ISTAR (see **b**)

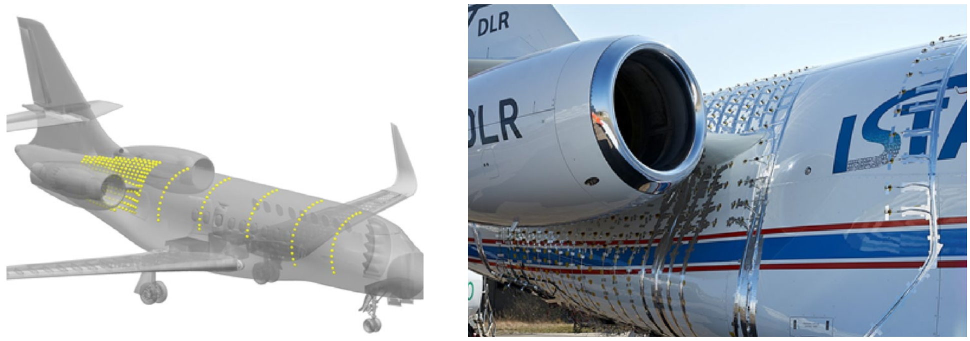

(a) Engine configuration plan

(b) Engine configuration realized ©2022DLR

Fig. 3 Sensor configuration used for the engine test. The engine runs were conducted with a configuration of 275 sensors (see **a**). The installation required every sensor and cable to be secured, prohibiting a roving grid method

In a measurement campaign lasting 2 weeks, vibration responses of the DLR ISTAR were acquired at 1350 positions. Additionally, engine induced vibrations were measured at 275 positions. The data cover the low-to-mid-frequency range and are of sufficient quality for planned work in FE model updating. In addition, first calculations of energy transfer paths using STI were conducted. These do not show a lot of surprises in the low-frequency range, but that was mostly to be expected. The fact that the STI calculation is possible and showing an intuitively viable energy flow field proves the experimental data to be of good quality and sufficient spatial resolution.

2.2 Principle operational deflection shapes

Principle Component Analysis (PCA) is becoming a more and more common tool in the field of experimental vibration analysis [6], where it finds extensive use with the advent of ever bigger data sets. The approach used within the context of this work is similar to the calculation of Principle Field Shapes (PFS, which are in fact the Principal Components or PCs) presented by Tengzelius [7].

The dominant vibrational behavior of a complex system within a limited frequency band where the modal density is too high to allow for the use of experimental modal analysis is calculated using PCA

$$\left[H_{Band}\right]_{n_S \times n_F} = [U]_{n_S \times n_S} [\Sigma]_{n_S \times n_F} [V]^H_{n_F \times n_F} . \tag{1}$$

$[H_{Band}]$ is a matrix of frequency response functions limited to a given frequency band of n_F frequency bins and n_S sensor positions. $[U]$ and $[V]$ are the left and right singular vector matrix and $[\Sigma]$ is a rectangular diagonal matrix containing corresponding singular values. Using the Singular Value Decomposition (SVD) algorithm, Eq. 1 can be solved numerically. While Tengzelius [7] directly used the resulting PCs per frequency band as a basis for FE model updating by comparing all experimental and simulated PCs per frequency band, for this work, a sum of PCs weighted individually by their statistical contribution to the overall response shape (i.e., ratio of variance) is calculated. This results in an approximated Principle Operational Deflection Shape (PODS) as representation of the response within the given frequency band. By calculating the projection of $[H_{Band}]$ to the basis $[V]$, the principle shapes $[PS]$ are obtained

$$[V]_{n_F \times n_F} \left[H_{Band}\right]_{n_F \times n_S} = [PS]_{n_F \times n_S} . \tag{2}$$

By normalizing the vector of diagonal elements of $[V]$, a ratio of participation per principle shape is acquired. All PSs up to a predetermined sum are weighted by this value and then added up to calculate the PODS to represent the structural response in the given frequency band.

2.3 Experimental structural intensity estimation

Structural Intensity (STI) is a vectoral quantity describing the vibrational power flow per unit areas through a structure. The STI is calculated by utilizing nodal velocities and rotations with the stresses acting in the elements. By multiplying the STI or the element stresses with the cross-sectional area in flow direction, it is possible to acquire the power flow in the unit Watt directly. The power flow for plate elements in x- and y-direction while neglecting the z-direction (thickness of the plate) can be described by

$$P_{x,s} = -\tfrac{1}{2} Re\left\{ N_{x,s} v_x^* + N_{xy,s} v_y^* + M_{x,s} \omega_y^* + M_{xy,s} \omega_x^* + Q_{xz,s} v_z^* \right\} \tag{3}$$

and

$$P_{y,s} = -\tfrac{1}{2} Re\left\{ N_{y,s} v_y^* + N_{xy,s} v_x^* + M_{y,s} \omega_x^* + M_{xy,s} \omega_y^* + Q_{yz,s} v_z^* \right\} \tag{4}$$

with N_i—normal element forces, M_i—element bending moments, Q_i—element transversal forces, v_i^*—complex conjugated nodal velocities, ω_i—nodal rotation speeds and the sub-index s indicating the values for shell elements [1]. All values and also the resulting intensities are time-averaged and frequency-dependent values. On the other hand, the power flow for beam elements can be described by

$$P_b = -\frac{1}{2}Re\left\{N_{x,b}v_x^* + T_b\omega_x^* - M_{y,b}\omega_y^* + M_{z,s}\omega_z^* + Q_{xz,b}v_z^* + Q_{xy,b}v_y^*\right\}, \tag{5}$$

with T_i—torsion along beam and the sub-index b indicating the values for beam elements [8].

To calculate the STI values, it is necessary to have information regarding nodal translation and rotation quantities as well as the forces or tensions acting in the structure. While, for FE models, this information are easily accessible, because they can be calculated for the most complex of structures. However, when it comes to calculating STI values based on experimental data, this becomes more difficult.

During experiments usually only, the outer velocity or acceleration field normal to the surface of structures can be measured. This means that nodal rotations as well as tensions are missing to calculate the STI values. One commonly used approach is to calculate the structures' tensions in discrete points by utilizing the Central Difference Method (CDM) which calculates the necessary derivatives of the displacement field by recursive operations [9]. This approach, however, has some drawbacks as it is only applicable on equidistant meshes, higher order derivatives result in progressing errors, and there is a need for higher evaluation space as the higher order derivatives need several measurement points aligned.

An alternative method based on the utilization of the FEM process [1, 10] overcomes these drawbacks and also makes it easy to extend the evaluation of structures for different element types. The measured field quantities are projected onto a mesh defined by the geometric sensor locations of the experimental setup. Therefore, the measurement grid needs to be of sufficient resolution to capture the structures' wavelength in the frequency range of interest. Based on this mesh, two sets of shape functions are created. The first set is utilized to approximate missing rotational quantities of the nodes. The second set is used in combination with a material law, in this case linear elastic behavior, and given material properties, in this case aluminum. This second set of shape functions allows to calculate forces and moments on element level. Necessary input values for the calculation with both shape function sets are the measurement data acquired with the sensors.

This approach allows to calculate STI fields for different elements based on the same field quantities acquired by measurements. For example, for light-weight structures which consists of bar-like frames covered with thin skins, STI values can be calculated on shell elements representing the skins and on beam elements representing the frame. Overlaying the results of these two vector fields results in a combined STI field carrying more information.

3 Results

3.1 Data quality

To get a good estimation of the quality of data measured, the standard deviation was calculated for the sensors fixed to the structure during all measurement runs of the roving grid measurements. If everything was exactly the same during each run, the deviation should be zero. This is, of course, not the case. The roving sensors are at different positions, the shakers push–pull rods had to be reattached and the environmental conditions like temperature can differ a bit. It was shown previously [3] that despite all these influences, the results, especially in the lower frequency range, can be quite good, with standard deviations calculated for 2σ intervals well below 20% and phase deviations below 10°. As was shown, while these numbers seem high, EMA is still easily possible in the low-frequency range and due to high modal density EMA is not an option in the higher frequency range.

For the data acquired during the ISTAR campaign is shown in Fig. 4. As can be seen, it is generally of the same quality as what was achieved in previous measurement campaigns utilizing the roving grid method in a large-scale test. In Fig. 4, the deviation of a single representative sensor is shown both for the FRF and for the results of the PCA-based averaging method (see 2.2). As is expected, the deviation for the third-octave band averaged data is significantly lower and preferable to get a rough overview of the structural behavior. To access the exact response to the tonal vibration input of the engines; however, the highly resolved FRF data will be used.

3.2 Principle operational deflection shapes

When dealing with mid-to-high-frequency vibrational responses, the modal density is very high. The vibrational behavior is hard to separate, resonance peaks tend to overlap heavily, and modal analysis is no longer possible. In fact, for frequencies of 80 Hz and up, experimental modal analysis cannot be successfully performed on the ISTAR data. Thus, the modal density cannot be determined. This was expected and is in accordance to earlier tests performed on full-size aircraft components ([2, 3]) where a full modal model could not be identified for frequencies above 80 Hz.

Using the PCA method (see 2.2), the dominating vibrational response in a given frequency band can be extracted

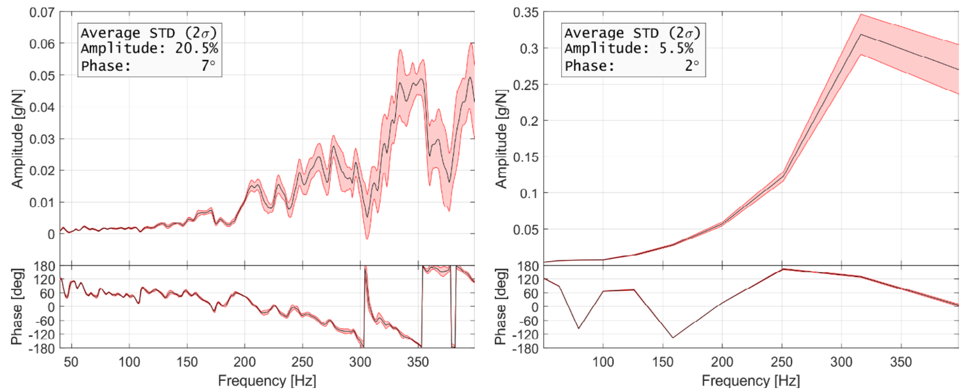

(a) Deviation of the sensor calculated directly using the frequency response functions

(b) Deviation of the same sensor as in 5a after application of PCA-based band averaging.

Fig. 4 Standard deviation calculated in a 2σ interval of a sensor present during all five configurations (see Fig. 3b). This sensor is located at the middle of the fuselage and its deviation in amplitude and phase representative for all fixed sensors

and used as a good approximation for the behavior in the analyzed frequency band. Usually, third-octave bands are used in the vibroacoustic analysis of broadband spectral excitation, giving an ever-broader band with rising frequency. An example for the 100 Hz band is shown in Fig. 6a.

The focus of this work is the analysis of vibration transport originating from tonal excitation as produced by the engines. The PCA method was used to get a narrow band approximation of the vibration response of the structure at engine excitation frequencies. The excitation frequencies of the engines were extracted from ground test data acquired with running engines. As stated above (see 2.1), the engine excitation data are limited in number of sensors. For the moment, the data were used only to extract the exact vibrational excitation frequencies. Future work aims to extend the data to the full aircraft using an updated numerical model.

For the analysis presented here, the PCA method was used to get a representative operational deflection shape for bands of ± 2.5 Hz around specific tonal excitation caused by the engine. The spectrum acquired during engine excitation runs with a sensor close to the pylon is shown in Fig. 5.

The resulting PODS were calculated using data acquired with artificial shaker excitation at the pylon. These data should be comparable to direct engine excitation. The resulting PODS at engine tonal frequencies are shown in Fig. 6a, b and c.

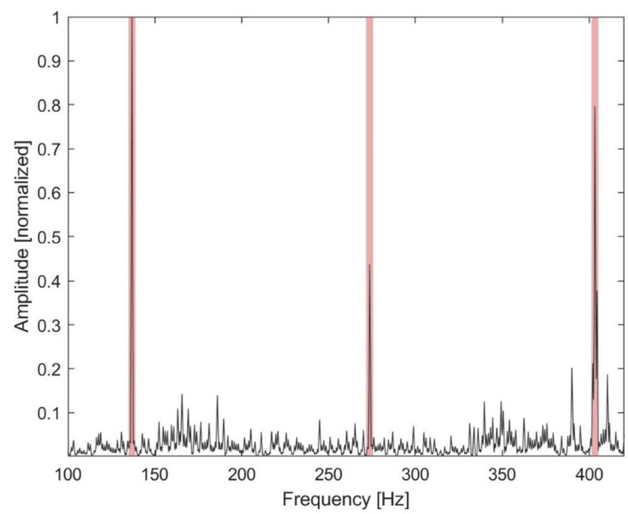

Fig. 5 Vibration input of the engines into the fuselage at pylon position. The shaded areas are at ± 2.5 Hz around the engine's tonal inputs

3.3 Transport of vibrational energy

To visualize the transport of vibrational energy, experimental STI is a very useful tool. Using the method described in Sect. 2.3, surface acceleration or velocity data can be used to estimate the power flow through a tested structure. There are several limitations; however, all of them readily apparent when looking at the analyzed data. The resulting STI only allows the analysis and visualization of measured areas of the structure. This seems like a trivial observation but always has to be kept in mind when looking at the resulting vector fields. When a full or at least mostly complete set of data are available, as was for example the case in [11], the power flow can be tracked through the structure and even the cavity encompassed by the structure. More often than not that is not the case. Instead, the STI analysis gives an incomplete picture of the power flow through the structure. Transfer of energy through parts of the structure which have not or could not be measured can only be estimated using engineering judgment or, if available, additional numerical data.

Using discrete Hodge–Helmholtz decomposition on the STI field, the net power flow represented by the divergent

Fig. 6 PODS for shaker excitation at pylon position at engine tonal frequencies

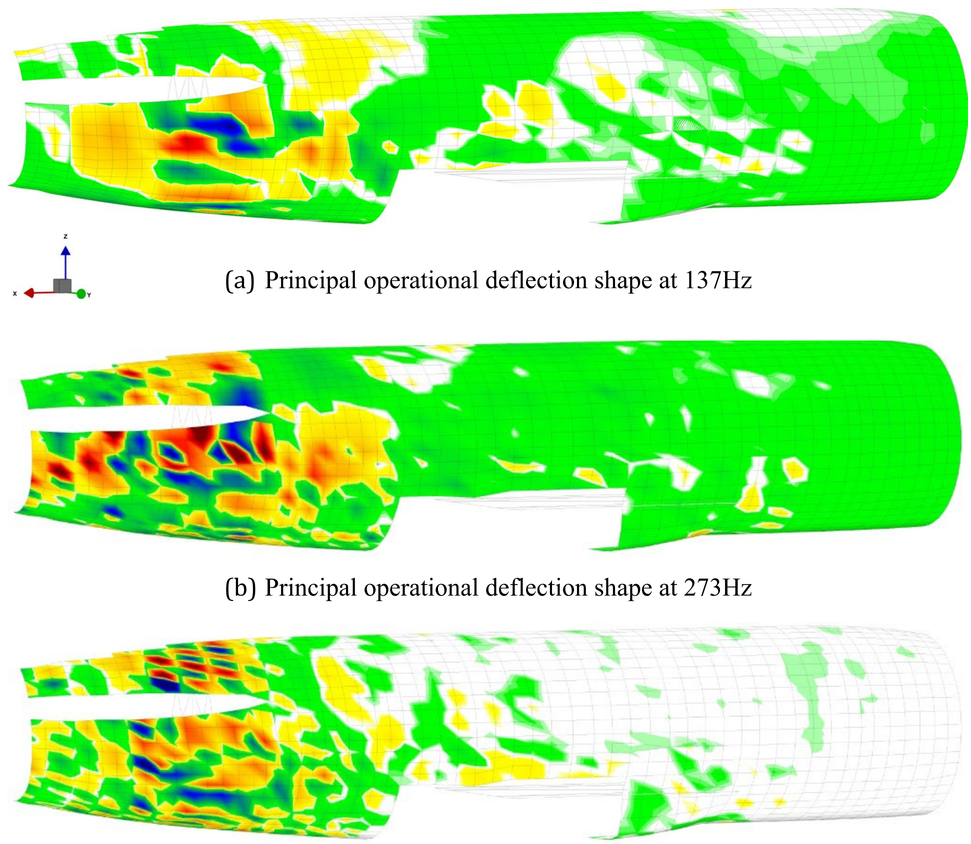

(a) Principal operational deflection shape at 137Hz

(b) Principal operational deflection shape at 273Hz

(c) Principal operational deflection shape at 403Hz

vector field can be separated from the rotational, sometimes called imaginary or solenoidal, part of the vector field. Recombining both would result in the original STI vector field [12, 13]. Each component carries vital information about the structure's vibrational behavior. The divergent field shows the connections of power sources and sinks. This is easiest to see when a simple, single point power source (i.e., a shaker attached to the fuselage) is used. The power flows from the source and is distributed over the surface toward energy sinks (see [1]). The rotational field is defined by not having any sinks or sources, rather showing the energy that is 'trapped' in the structure's resonant properties. It is thus strongly linked to modal behavior in the given frequency range.

Presented here are four sets of STI evaluations. As detailed above, these represent the STI vector fields for the third-octave band centered around 100 Hz as well as 5 Hz bands centered on the primary engine excitation frequencies at 137 Hz, 273 Hz, and 403 Hz. The limit of the picked frequencies was set by the range present during shaker excitation of 40–500 Hz.

As stated above, the data used for analysis were acquired by shaker excitation at the pylon. While the engine excitation was measured in detail using dense grid of 275 positions, this is nowhere close to the 1300 positions measured using shaker excitation.

Figure 7 shows the PODS and STI data for the third-octave band centered around 100 Hz. These data, being the result of a wide band averaging, give a good baseline for the best-case vector fields that could be extracted from the data. The PODS in Fig. 7a shows a vibration response that is centered on the pylon. Below the pylon, some skin fields seem to be in resonance. Some windows above the wing also show clear resonant behavior. Extracting any kind of power flow from this would be close to impossible. The STI analysis of the divergent vector field (Fig. 7b) shows the energy originating just below the pylon. The high amplitudes above seem to not participate in the power flow. This will most likely be through the heavily enforced frame the pylon is attached through. The power is than more or less evenly flowing from the power input over the fuselage. The rotational vector field (Fig. 7c shows some power vortexes around the area under the pylon and around the rear end of the fuselage, giving a good representation for the resonant behavior shown in the PODS.

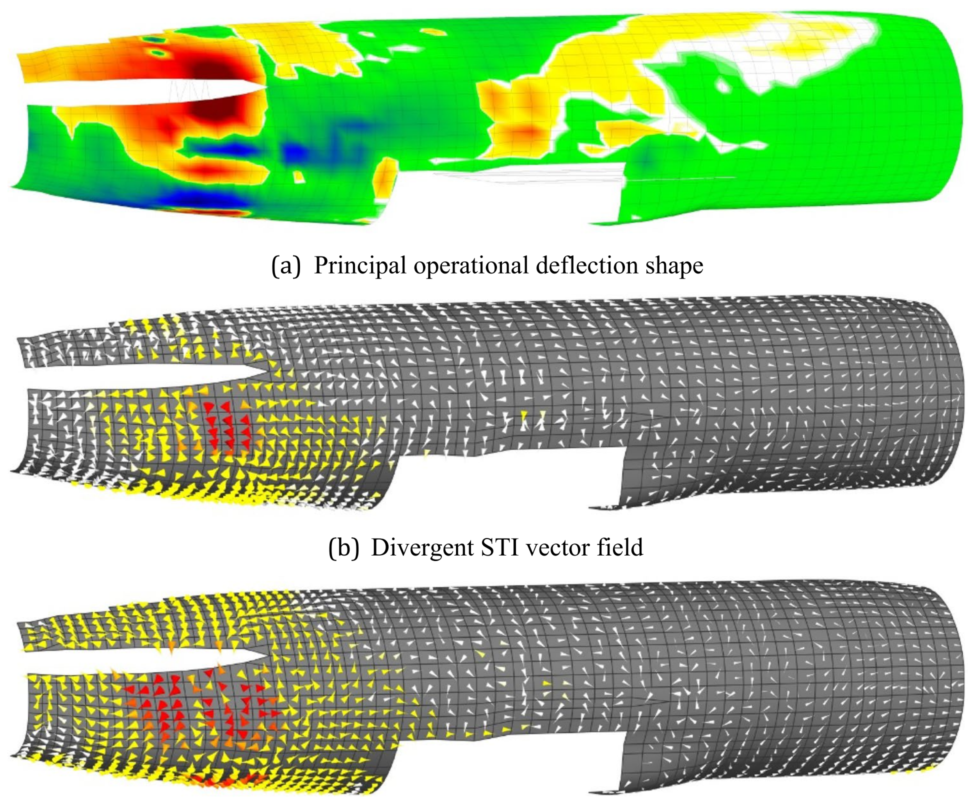

(a) Principal operational deflection shape

(b) Divergent STI vector field

(c) Rotational STI vector field

Fig. 7 Operational deflection shape and decomposed STI fields for the 100 Hz 1/3-octave band (89–112 Hz) for excitation at pylon position

The narrow band PODS acquired at engine tonal frequencies are shown in Fig. 8. It is obvious and was expected that the results differ a lot between the three picked tonal frequencies at 137 Hz, 273 Hz, and 403 Hz. With increasing frequencies, local behavior begins to dominate the vibrational response. A reduction in response amplitudes from pylon position in the back to the front is still discernible, but a clear transfer path cannot be seen in this depiction of the data.

Despite the strong differences in local vibrational behavior, the resulting STI patterns are quite similar. Comparing divergent vector field results for all three excitation frequencies as done in Fig. 8 shows the power flow to be remarkably similar between all three input frequencies. The main power source is, similar to the broad band analysis above, the pylon structure used for excitation and the frame directly attached to the pylon. The strongest power sink in the visible area is in the direct vicinity of the power source. The energy seems to reenter the inner structure at the point of highest curvature at the two frames connected to the pylon. Given this observation, two important facts about the analysis need to be kept in mind: By definition, the STI field is incomplete showing only the power flow where sensors are present. Where the power flowing from the front of the fuselage toward the back is originating can only be guessed. Most likely via the inner structure of the aircraft. The pylon frames and the pressure bulkhead come to mind as possible short circuits. If that is the case, it is not readily apparent with the data at hand.

The corresponding rotational STI vector fields are shown in Fig. 9. By definition, the rotational vector fields should be perpendicular to the divergent fields in Fig. 8 and correspond to energy to circulate within the structure. A close look at these reveals them to have more significant differences than the vector fields acquired for the divergent component of the STI. The radial power flow, for example, in the front of the fuselage is clockwise for the 273 Hz operational deflection shape (Fig. 9b) but counterclockwise for the 137 Hz and 403 Hz shapes (Fig. 9a and c). Similarly, the local vortexes formed at and around the pylon where the excitation is highest differ greatly between the three shown vector fields. This is not surprising as they should correspond to the different

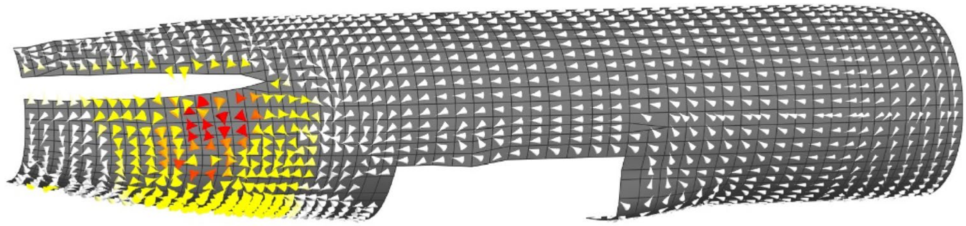

(a) Divergent STI vector field at 137Hz

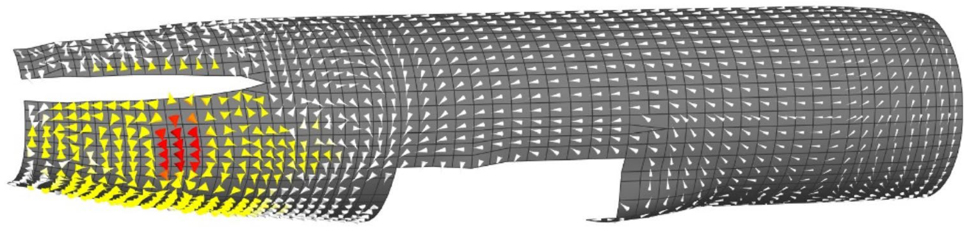

(b) Divergent STI vector field at 273Hz

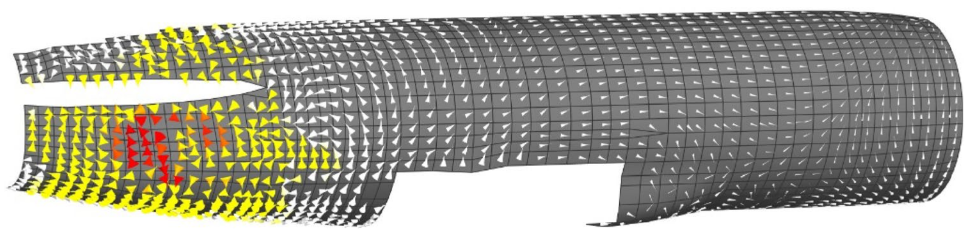

(c) Divergent STI vector field at 403Hz

Fig. 8 Divergent STI fields for shaker excitation at pylon position at engine tonal frequencies

resonant behavior of the structure as shown by the individual PODS in Fig. 6.

4 Summary and conclusion

As a result of a 2-week measurement campaign on DLRs Falcon 2000LX ISTAR, detailed vibrational response data were acquired at more than 1300 measurement points. The experimental data are of sufficient quality to allow for STI analysis. This processing method gives detailed information about the transport of vibrational energy along the fuselage surface. It was conducted using PODS, principle operational deflection shapes, which show the dominating response in a given frequency band. The STI analysis was performed both using third-octave bands and PODS centered in a narrow band around the engine excitation frequencies, all using artificial shaker excitation at the pylon.

The operational deflection shapes show strong differences depending on the width of the frequency band and the center frequency of the band they represent. This is, of course, no surprise and in full alignment with expectations. The same can be said for the rotational vector field representing the resonant behavior of the examined operational deflection shape. The divergent STI vector field, on the other hand, is mostly the same or at least strikingly similar no matter what bandwidth or frequency is used for the analysis. This suggests that, for the analyzed structure, the transport of vibrational energy follows mostly the same path in the mid-frequency range of 100 Hz to 500 Hz. This observation is different to what has been seen in other similar experiments [1, 2, 14], where large differences in transport paths were examined depending on the frequency observed. Those tests were performed with less strongly damped structures, suggesting that with highly damped structures, the energy transport paths become more stable and less dependent on the frequency or exact excitation position.

Fig. 9 Rotational STI for shaker excitation at pylon position at engine tonal frequencies

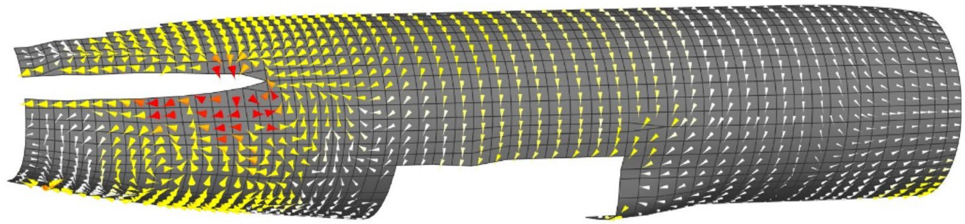

(a) Rotational STI vector field at 137Hz

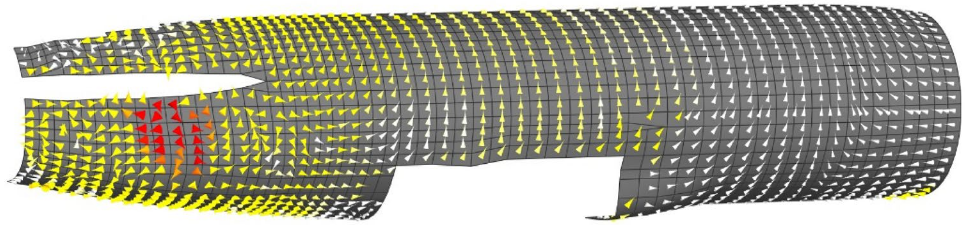

(b) Rotational STI vector field at 273Hz

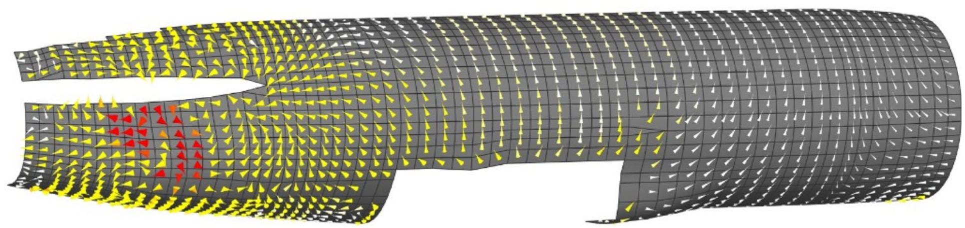

(c) Rotational STI vector field at 403Hz

Funding Open Access funding enabled and organized by Projekt DEAL. The research leading to these results received funding from the Clean Sky 2 Joint Undertaking under the European Union's Horizon 2020 research and innovation program under Grant Agreement No. CS2-LPA-GAM-2020-2023-01.

Declarations

Conflict of interest The authors have no competing interests to declare that are relevant to the content of this article.

References

1. Biedermann, J., Winter, R., Norambuena, M., Bswald, M.: A hybrid numerical and experimental approach for structural intensity analysis of stiffened lightweight structures. In: Proc. Int. Conf. Noise Vib. Eng., Int. Conf. Uncertain Struct. Dyn., pp. 4101–4115 (2018)
2. Winter, R., Biedermann, J., Norambuena, M.: High-resolution vibration measurement and analysis of the Flight-LAB aircraft fuselage demonstrator. In: Proceeding of INTER-NOISE 2018 (2018)
3. Winter, R., Biedermann, J., Böswald, M., Wandel, M.: Dynamic characterization of the A400M acoustics fuselage demonstrator. In: Proceeding of INTER-NOISE 2016, pp. 3296–3306 (2016)
4. Winter, R., Sinske, J., Norambuena, M., Zettel, S.F.: High-resolution vibroacoustic measurement and analysis of the DLR ISTAR aircraft to assess engine-induced cabin noise. In: Proceeding of INTER-NOISE 2022 (2022)
5. Govers, Y., Sinske, J., Petzsche, T.: Latest design trends in modal accelerometers for aircraft ground vibration testing. In: Walber, C., Walter, P., Seidlitz, S. (eds.) C Proc Soc Exp Mech,

pp. 97–106. Springer, Cham (2020). https://doi.org/10.1007/978-3-030-12676-610
6. Allemang, R.J., Phillips, A.W., Allemang, M.R.: Application of principal component analysis methods to experimental structural dynamics. In: Proulx, T. (ed.) C. Proc. Soc. Exp. Mech., pp. 477–498 (2011). https://doi.org/10.1007/978-1-4419-9834-7
7. Tengzelius, U., Horlin, N., Emborg, U., Gustavsson, M., der Auweraer, H.V., Iadevaia, M.: Correlation of medium frequency test and FE models for a trimmed aircraft test section. In: Aeroacoustics Conf., p. (1998). https://doi.org/10.2514/6.1998-2307
8. Hambric, S.A.: Power flow and mechanical intensity calculations in structural finite-element analysis. J. Vib. Acoust. **112**(4), 542–549 (1990). https://doi.org/10.1115/1.2930140
9. Williams, E.G., Dardy, H.D., Fink, R.G.: A technique for measurement of structure-borne intensity in plates. J. Acoust. Soc. Am. **78**, 2061–2068 (1985). https://doi.org/10.1121/1.392663
10. Pires, F., Avril, S., Vanlanduit, S., Dirckx, J.: Structural intensity assessment on shells via a finite element approximation. J. Acoust. Soc. Am. **145**(1), 312–326 (2019). https://doi.org/10.1121/1.5087564
11. Biedermann, J., Winter, R., Norambuena, M., Wandel, M.: Räumlich hochauflösende vibroakustische Messung zur Charakterisierung eines Kurzstreckenflugzeugrumpfs im mittleren Frequenzbereich. In: Dt. Luft Raumf. Kong. (2018)
12. Polthier, K., Preuß, E.: Identifying vector field singularities using a discrete hodge decomposition. In: Visualization and mathematics. Springer, Verlag (2003)
13. Lamarsaude, B., et al.: Structural intensity analysis for car body design: going beyond interpretation issues through vector field processing. Proceedings of the ISMA. (2014)
14. Winter, R., Heyen, S., Biedermann, J.: Experimental structure intensity analysis of an Airbus A400M fuselage structure using high-resolution vibration measurements. In: Int. Congr. Acoust. Int. Congr. Acoust., pp. 8118–8125 (2019). https://doi.org/10.18154/RWTH-CONV-239044